Journal of Rock Mechanics and Geotechnical Engineering 15 (2023) 1520–1534

Contents lists available at ScienceDirect

Journal of Rock Mechanics and Geotechnical Engineering

journal homepage: www.jrmge.cn

Full Length Article

Modeling pipe-soil interaction under vertical downward relative offset using B-spline material point method

Chunxin Zhang [a], Honghu Zhu [a,b,*], Haojie Li [a]

[a] School of Earth Sciences and Engineering, Nanjing University, Nanjing, 210023, China
[b] Institute of Earth Exploration and Sensing, Nanjing University, Nanjing, 210023, China

ARTICLE INFO

Article history:
Received 8 May 2022
Received in revised form
23 June 2022
Accepted 17 July 2022
Available online 15 August 2022

Keywords:
Pipe-soil interaction
Material point method (MPM)
Large ground deformation
Failure mechanism
Downward movement

ABSTRACT

To analyze the pipeline response under permanent ground deformation, the evolution of resistance acting on the pipe during the vertical downward offset is an essential ingredient. However, the efficient simulation of pipe penetration into soil is challenging for the conventional finite element (FE) method due to the large deformation of the surrounding soils. In this study, the B-spline material point method (MPM) is employed to investigate the pipe-soil interaction during the downward movement of rigid pipes buried in medium and dense sand. To describe the density- and stress-dependent behaviors of sand, the J_2-deformation type model with state-dependent dilatancy is adopted. The effectiveness of the model is demonstrated by element tests and biaxial compression tests. Afterwards, the pipe penetration process is simulated, and the numerical outcomes are compared with the physical model tests. The effects of pipe size and burial depth are investigated with an emphasis on the mobilization of the soil resistance and the failure mechanisms. The simulation results indicate that the bearing capacity formulas given in the guidelines can provide essentially reasonable estimates for the ultimate force acting on buried pipes, and the recommended value of yield displacement may be underestimated to a certain extent.

1. Introduction

The relative movement between the pipeline and surrounding soil commonly occurs under permanent ground deformation, which may arise from slope instability, normal or oblique fault movement, tunnel excavation and other detrimental geotechnical conditions (Akhtar and Li, 2020; Wang et al., 2021). The pipeline strain and curvature caused by this relative motion are generally calculated analytically or numerically using nonlinear beam-spring models (ALA, 2005; Kouretzis et al., 2015; Yao et al., 2021). In these models, the force–displacement relationships of the axial, lateral and vertical elastoplastic springs are necessary input parameters to represent the reaction force of the surrounding soil during relative soil-pipe movement. The vertical bearing Winkler springs have a significant impact on the structural response of the pipeline compared to the lateral and vertical uplift soil springs. This is because the soil resistance acting on the pipe subjected to vertical downward movement is considerably higher than that under relative movement in other directions (Jung et al., 2016; Wu et al., 2021; Li et al., 2022). However, the majority of researches related to soil springs were focused on the lateral and vertical uplift offset conditions, with less attention given to the vertical downward offsets.

The current design guidelines (ALA, 2005; PRCI, 2009) recommend using the common bearing capacity formulas proposed for the shallow strip footing problem to estimate the maximum force developing on the pipe during the vertical downward offset. Some numerical results challenge the accuracy of these bearing capacity formulas in predicting the ultimate resistance of the surrounding soil. Jung et al. (2016) and Qin et al. (2019) performed a series of finite element (FE) analyses and noted that the conventional bearing capacity equations prominently overestimated the ultimate resistance. In this case, Qin et al. (2019) proposed that the appropriate reduction of the friction angle of sand combined with the design equation recommended by ALA (2005) can provide the upper and lower bounds of the bearing capacity. Notably, FE modeling inevitably encounters computational difficulties in case of large soil

* Corresponding author. School of Earth Sciences and Engineering, Nanjing University, Nanjing, 210023, China. .
E-mail address: zhh@nju.edu.cn (H. Zhu).
Peer review under responsibility of Institute of Rock and Soil Mechanics, Chinese Academy of Sciences.

https://doi.org/10.1016/j.jrmge.2022.07.010

deformations near the pipe (Kouretzis and Bouckovalas, 2019; Limnaiou et al., 2019). The soil resistance response was investigated within a relatively small pipe offset in the FE simulations (Jung et al., 2016; Qin et al., 2019), probably due to the limitation of excessive element deformations. This insufficient pipe movement may lead to the inadequate mobilization of soil resistance and a more conservative estimation of ultimate resistance. Moreover, Kouretzis et al. (2014) investigated the maximum bearing force acting on pipes and the failure mechanism of the surrounding soil using the finite element limit analysis (FELA) method. Nevertheless, this FELA method cannot obtain the evolution of resistance with the progressive failure of the soil. Recently, Wu et al. (2021) performed 1g physical model tests of the vertical penetration of rigid buried pipes to explore the characteristics of bearing springs and the failure mechanisms in sands with various densities. It is beneficial for understanding the bearing spring properties to explore the soil resistance and progress failure modes using more advanced numerical models benchmarked by the test results.

The recently developed material point method (MPM), a combination of Eulerian and Lagrangian formulations, can effectively avoid mesh tangling in the pure Lagrangian method under large deformations (Sulsky et al., 1995). Based on the advantage of large deformation analyses and the straightforward contact algorithm proposed by Bardenhagen et al. (2000), this numerical method has been extensively validated for geotechnical problems involving the progressive and post-failure process of soils (Bandara and Soga, 2015; Bhandari et al., 2016) and the soil-structure interaction (Phuong et al., 2016; Zhang et al., 2022). To accurately simulate the process of pipe penetration into soils, it is essential to overcome the grid-crossing errors resulting from the jump discontinuity in the gradient of piecewise-linear shape functions in the standard MPM. Several advanced approaches have been proposed to mitigate these issues, such as the generalized interpolation material point (GIMP) method (Bardenhagen and Kober, 2004), in which the characteristic function is introduced to construct the particle domain; the dual domain material point (DDMP) method (Zhang et al., 2011), in which the gradient of the shape functions is modified and smoothed; and the B-spline material point method (BSMPM) (Steffen et al., 2008; Gan et al., 2018), in which higher-order nodal shape functions are adopted. The present MPM simulations are performed using the BSMPM, which has been proven to improve the numerical solution accuracy and spatial convergence (Steffen et al., 2010).

The selection of a suitable constitutive model is the key to reflecting the response of the surrounding soil during pipe penetration. In this process, the stress and void ratio of the soil around the pipe undergo quite variable changes. Therefore, a robust and easy-to-implement constitutive model is required to characterize the state evolution of soil. The J_2-deformation type model with state-dependent dilatancy proposed by Yang et al. (2019) is adopted as the soil constitutive model in this study. The capability and robustness of this model have been verified through triaxial element tests and typical boundary value problems such as strip footing tests (Yang et al., 2019; Liao et al., 2021). The prominent advantage of the J_2 model is that the essential features of the soil (i.e. the nonlinear stress–strain relationship, strain-softening, state-dependent dilatancy and critical state failure) can be well captured with relatively succinct concepts and fewer model parameters. Afterwards, an extended scheme accounting for fabric evolution was implemented in FE analysis and applied to investigate the response of strip footing on anisotropic sand (Liao and Yang, 2021). This extension has not been considered in the present analyses due to the less significant anisotropy of the backfill sand around the pipe.

In this paper, a series of numerical simulations is performed to model the pipe penetration process in sand using the BSMPM combined with the J_2-deformation type model. After a brief introduction to the numerical framework, a series of element tests and biaxial compression tests are simulated to validate the effectiveness of the constitutive model implemented in MPM. The benchmark simulations of the pipe-soil interaction are carried out at the same scale as the laboratory tests reported by Wu et al. (2021), and the numerical results are compared with the corresponding test results. The embedment condition of the dense and medium sand is considered as its relative densities are closer to the practical backfill state. Afterwards, the effects of pipe diameter and burial depths are investigated with particular attention to the mobilization of the soil resistance and the failure mechanisms. Finally, the calculated bearing capacity based on force–displacement curves is compared with the widely used design guidelines and previous experimental and numerical results, which provides improved insight into the soil response during vertical downward pipe offset.

2. Numerical method

2.1. Basic solution scheme of MPM

The MPM is a hybrid Lagrangian–Eulerian approach and originates from the extension formulation of Particle-in-Cell (PIC) for solid mechanics (Sulsky et al., 1995). In MPM, the continuum bodies are discretized into a series of Lagrangian particles/material points (MPs), which store all the physical information (i.e. mass m_p, position $\boldsymbol{x}_p$, velocity $\boldsymbol{v}_p$, stress $\boldsymbol{\sigma}_p$, etc.), material parameters and other state parameters. Meanwhile, the Eulerian background grid covering the MP motion domain is constructed to solve the momentum balance equation. The computational information required on the background grid is transferred from the MPs through shape functions, and then the mesh results are mapped back to the MPs to update the carried information.

Following the explicit MPM procedure with the modified-update-stress-last (MUSL) scheme (Zhang et al., 2017), at the beginning of this process, the grid nodal mass m_I and momentum $\boldsymbol{p}_I$ are obtained by mapping the particle mass and momentum to the corresponding grid nodes:

$$m_I^k = \sum_{p=1}^{n_p} m_p N_{Ip}^k \tag{1}$$

$$\boldsymbol{p}_I^{k-1/2} = \sum_{p=1}^{n_p} m_p \boldsymbol{v}_p^{k-1/2} N_{Ip}^k \tag{2}$$

where superscript k indicates the time step; subscripts p and I indicate the particle index and the grid node index, respectively; n_p is the total number of particles; and N_{Ip} is the shape function associated with grid node I evaluated at the position of particle p. The positions and velocities are updated at interleaved time points due to the adoption of the central difference method. The tensors and vectors are denoted with bold font if they are not expressed as indicial forms.

The grid nodal internal force $\boldsymbol{f}_I^{\mathrm{int},k}$, external force $\boldsymbol{f}_I^{\mathrm{ext},k}$ and total grid nodal force $\boldsymbol{f}_I^k$ are then given as

$$\boldsymbol{f}_I^{\mathrm{int},k} = -\sum_{p=1}^{n_p} \nabla N_{Ip}^k \boldsymbol{\sigma}_p^k V_p^k \tag{3}$$

$$\boldsymbol{f}_I^{\mathrm{ext},k} = \sum_{p=1}^{n_p} m_p N_{Ip}^k \boldsymbol{b}_p^k + \sum_{p=1}^{n_{bp}} N_{I(bp)}^k \bar{t}_{bp}^k \frac{S_{el}}{n_{bp}} \tag{4}$$

$$\boldsymbol{f}_I^k = \boldsymbol{f}_I^{\text{int},k} + \boldsymbol{f}_I^{\text{ext},k} \tag{5}$$

where $\boldsymbol{\sigma}_p$ is the stress of particle p, V_p is the volume associated with particle p, $\boldsymbol{b}_p$ is the body force, n_{bp} is the number of boundary particles bp, $\bar{t}_{bp}^k$ is the specific traction at the position of boundary particle bp, and S_{el} is the traction surface of the boundary element.

The grid nodal momentum $\boldsymbol{p}_I^{k+1/2}$ is updated by integrating the momentum equation:

$$\boldsymbol{p}_I^{k+1/2} = \boldsymbol{p}_I^{k-1/2} + \boldsymbol{f}_I^k \Delta t \tag{6}$$

where Δt is the time step determined by multiplying the critical time step by the Courant number. The particle velocity $\boldsymbol{v}_p^{k+1/2}$ and position $\boldsymbol{x}_p^{k+1}$ are updated through the grid nodal force and momentum:

$$\boldsymbol{v}_p^{k+1/2} = \boldsymbol{v}_p^{k-1/2} + \sum_{I=1}^{n_n} \frac{\boldsymbol{f}_I^k N_{Ip}^k}{m_I^k} \Delta t \tag{7}$$

$$\boldsymbol{x}_p^{k+1} = \boldsymbol{x}_p^k + \sum_{I=1}^{n_n} \frac{\boldsymbol{p}_I^{k+1/2} N_{Ip}^k}{m_I^k} \Delta t \tag{8}$$

where n_n is the total number of grid nodes related to the particles p. After updating the motion information of particles, the grid nodal momentum $\boldsymbol{p}_I^{k+1/2}$ is recalculated:

$$\boldsymbol{p}_I^{k+1/2} = \sum_{p=1}^{n_p} m_p \boldsymbol{v}_p^{k+1/2} N_{Ip}^k \tag{9}$$

After the calculation of grid nodal velocity with $\boldsymbol{v}_I^{k+1/2} = \boldsymbol{p}_I^{k+1/2}/\boldsymbol{m}_I^k$, the incremental strain tensor $\Delta\varepsilon_p^{k+1/2}$ and spin tensor $\Delta\Omega_p^{k+1/2}$ of particles are further computed to update the particle stress state and the volume V_p^{k+1} (Zhang et al., 2017). At this point, the deformed grid can be discarded, and the particles will carry all necessary information for the next time step.

2.2. BSMPM

The BSMPM follows the above solution scheme for the standard MPM, in which higher-order B-splines are adopted as shape functions. For the construction of the B-spline basis functions, a knot vector is introduced and denoted as a set of non-decreasing knot values $\Xi = \{\xi_1, \xi_2, \ldots, \xi_{n+h}, \xi_{n+h+1}\}$, where n and h are the number of basis functions and the polynomial order, respectively. For a given knot vector, the univariate B-spline basis functions of order h related to the ith knot, $\Phi_{i,h}$, are determined recursively according to the Cox-de Boor (1978).

The piecewise constants are defined for the zeroth order ($h = 0$) basis functions:

$$\varphi_{i,h}(\xi) = \begin{cases} 1 & (\text{if } \xi_i \le \xi < \xi_{i+1}) \\ 0 & (\text{otherwise}) \end{cases} \tag{10}$$

For $h \ge 1$, the basis functions are given following the recursion strategy:

$$\varphi_{i,h}(\xi) = \frac{\xi - \xi_i}{\xi_{i+h} - \xi_i} \varphi_{i,h-1}(\xi) + \frac{\xi_{i+h+1} - \xi}{\xi_{i+h+1} - \xi_{i+1}} \varphi_{i+1,h-1}(\xi) \tag{11}$$

where the convention of $0/0 = 0$ is made.

In the present MPM program, the knots are constructed on the nodes of the structured background grid, and the cubic (i.e. $h = 3$) B-spline basis function is employed. The knot vector of the internal nodes is different from that close to the boundary nodes because the first and last knots need to be repeated $h + 1$ times to make the B-spline interpolate accurately at the end points (Steffen et al., 2008; Gan et al., 2018). Fig. 1 shows the cubic B-spline basis functions and their gradient for a series of five elements, including the modification at the boundary. The multivariate B-spline basis functions are created by taking the tensor product of univariate basis functions. Further details about the BSMPM can be found in the relevant literature (e.g. Steffen et al., 2008; Gan et al., 2018).

2.3. Rigid contact algorithm

Based on the frictional contact algorithm proposed by Bardenhagen et al. (2000), the rigid contact algorithm (Zhang et al., 2017) that introduces a rigid body with prescribed motion information is adopted to model the pipe-soil interaction, as the pipe is generally treated as a rigid section and is subjected to a specific velocity boundary in the model tests (Trautmann, 1983; Wu et al., 2021). For the rigid body, the discretized particles only carry the mass and prescribed motion parameters to update their positions and solve the mass gradient to determine the contact surface. The

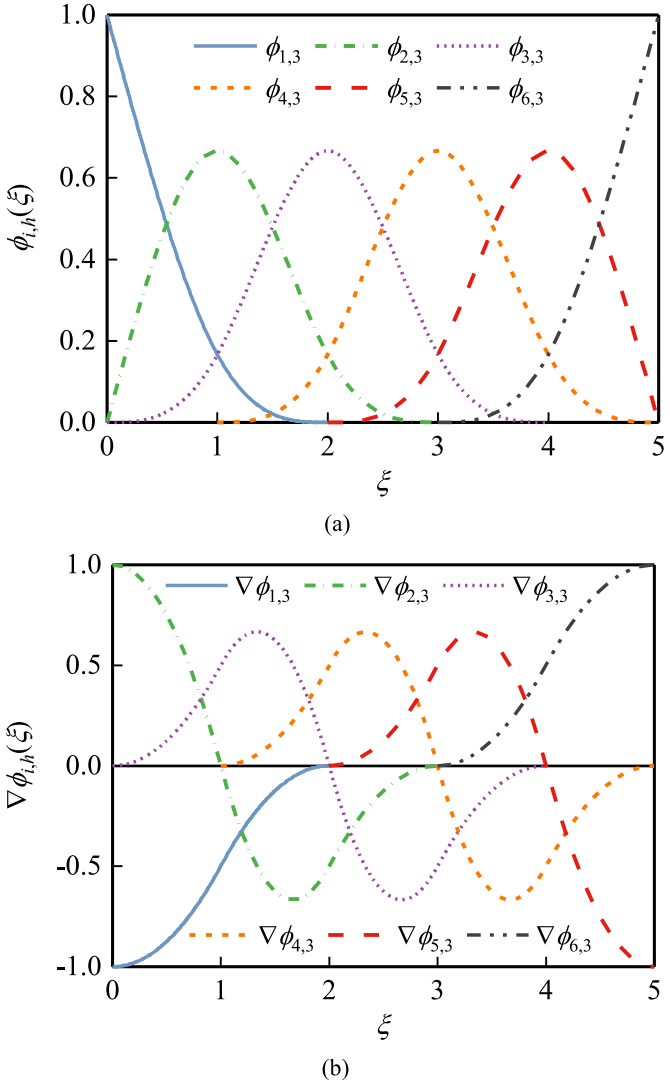

Fig. 1. Example of (a) Cubic B-spline basis functions and (b) Their gradient for a series of five equally spaced elements.

contact force is computed based on the impenetrability condition and the velocity fields of the rigid body and deformable body, which is only applied to the deformable body to correct its trial velocity. Further information on this calculation process can be found in the literature (Bardenhagen et al., 2000; Zhang et al., 2017).

Basically, the rigid contact algorithm is equivalent to a moving friction boundary carrying the time-dependent motion information (i.e. velocities and accelerations). In addition, this methodology also avoids the limitation of the low critical time step dominated by the Courant–Friedrichs–Lewy (CFL) condition (Courant et al., 1967) for a structure with large stiffness. A similar technique is applied to simulate the soil-structure interaction (Zhang et al., 2022) and the slope failure caused by seismic motion (Bhandari et al., 2016).

2.4. Soil constitutive model

The basic formulation of the J_2-deformation type model with state-dependent dilatancy is briefly presented in this section. For further detailed mathematical derivation and numerical implementation, one can refer to the literature (Yang et al., 2019; Liao et al., 2021). In the following expressions, the subscripts i, j and k (e.g. the stress tensor σ_{ij} and strain tensor ε_{ij}) indicate the spatial components following the Einstein summation convention. The deviatoric stress tensor can be expressed as $s_{ij} = \sigma_{ij} - p\delta_{ij}$, where δ_{ij} is the Kronecker delta ($\delta_{ij} = 1$ for $i = j$ and $\delta_{ij} = 0$ for $i \neq j$) and $p = \sigma_{kk}/3$ denotes the mean normal stress. The deviatoric stress is given by $q = \sqrt{(3/2)s_{ij}s_{ij}}$. The stress ratio tensor and stress ratio are expressed as $r_{ij} = s_{ij}/p$ and $\eta = q/p$, respectively. Similarly, the deviatoric strain tensor is expressed as $e_{ij} = \varepsilon_{ij} - \varepsilon_{kk}\delta_{ij}/3$, in which $\varepsilon_v = \varepsilon_{kk}$ denotes the volumetric strain, and $\varepsilon_q = \sqrt{(3/2)e_{ij}e_{ij}}$ is the deviatoric strain.

The stress–strain relation is described by the following expression (Yang et al., 2019):

$$q = \underbrace{\frac{\varepsilon_q}{a + b\varepsilon_q}}_{q'} + \underbrace{\left[\left(-\frac{\varepsilon_q}{\varepsilon_r}\right)Dp\exp\left(-\frac{\varepsilon_q}{\varepsilon_r}\right)\right]}_{q''} \tag{12}$$

where the first term q' indicates the hyperbolic relation between q and ε_q to reflect the nonlinear stress–strain relationship of soil, and the second term q'' is used to describe the softening behavior.

The parameters a and b in the term q' of Eq. (12) indicate the initial tangential stiffness and the ultimate failure strength of the soil, respectively, and are given as

$$a = \frac{1}{3G} \tag{13}$$

$$b = \frac{1}{M_c g(\theta)p} \tag{14}$$

where G is the elastic shear modulus dependent on the stress level and can be expressed as

$$G = G_0\frac{(2.973 - e_0)^2}{1 + e_0}\sqrt{pp_a} \tag{15}$$

where G_0 is a material constant, e_0 is the initial void ratio, and p_a is the atmospheric pressure (101 kPa). In Eq. (14), the interpolation function $g(\theta)$ about the Lode angle θ can be obtained according to Li (2002):

$$g(\theta) = \frac{\sqrt{(1 + c^2)^2 + 4c(1 - c^2)\sin 3\theta} - (1 + c^2)}{2(1 - c)\sin 3\theta} \tag{16}$$

which describes the smooth evolution from $g(\theta) = 1$ for triaxial compression ($\theta = -\pi/6$) to $g(\theta) = c$ for triaxial tension ($\theta = \pi/6$), with $c = M_e/M_c$ (M_e and M_c denote the critical stress ratios at triaxial extension and compression, respectively).

In the second term q'' of Eq. (12), the state-dependent dilatancy function D is employed according to Li and Dafalias (2000) to characterize the volumetric response during shearing:

$$D = \frac{d\varepsilon_v^p}{d\varepsilon_q^p} = d_0\left[\exp(m\psi) - \frac{\eta}{M_c g(\theta)}\right] \tag{17}$$

where d_0 and m are two model parameters, and the state parameter ψ is defined as

$$\psi = e - e_c \tag{18}$$

where e is the current void ratio, and the critical void ratio e_c is a function of the mean normal stress p and defined by Li and Wang (1998) as

$$e_c = e_\Gamma - \lambda_c(p/p_a)^\xi \tag{19}$$

where e_Γ, λ_c, and ξ are three material constants.

The increment of the plastic strain tensor $d\varepsilon_{ij}^p$ is calculated with

$$d\varepsilon_{ij}^p = \langle L\rangle\chi_{ij} = \langle L\rangle\left(n_{ij} + \frac{1}{3}\sqrt{\frac{2}{3}}D\delta_{ij}\right) \tag{20}$$

where $\langle L\rangle$ denotes the Macauley brackets with $\langle L\rangle = L$ when $L > 0$ and $\langle L\rangle = 0$ for $L \leq 0$; L is the loading index and obtained by $L = \sqrt{de_{ij}^p de_{ij}^p} = \sqrt{3/2}d\varepsilon_q^p$; χ_{ij} denotes the direction of $d\varepsilon_{ij}^p$, including a deviatoric part n_{ij} and a volumetric part $\frac{1}{3}\sqrt{\frac{2}{3}}D\delta_{ij}$. n_{ij} is determined through the direction of the stress ratio as

$$n_{ij} = \frac{r_{ij}}{\sqrt{r_{kl}r_{kl}}} \tag{21}$$

The loading index L can be obtained from Eq. (22) (i.e. the differential form of Eq. (12)) as follows:

$$dq = \frac{\partial q}{\partial p}dp + \frac{\partial q}{\partial e}de + \frac{\partial q}{\partial \varepsilon_q}d\varepsilon_q \tag{22}$$

$$L = \sqrt{\frac{3}{2}}\left\{\frac{[CK - E(1 + e_0)]}{(CKD - 3G)}d\varepsilon_v + \frac{(F - 3G)}{(CKD - 3G)}d\varepsilon_q\right\} \triangleq \Pi_{ij}\, d\varepsilon_{ij} \tag{23}$$

where $C = \partial q/\partial p$, $E = \partial q/\partial e$, $F = \partial q/\partial \varepsilon_q$, and K is the elastic bulk modulus and expressed as

$$K = \frac{(1 + e_0)p}{\kappa\xi}\left(\frac{p_a}{p}\right)^\xi \tag{24}$$

where κ is a material constant. The specific expressions of C, E, F, Π_{ij} and the loading index L can be found in Appendix A.

By combining Eqs. (20–24), the incremental stress–strain relation can be obtained as

$$d\sigma_{ij} = \Lambda_{ijkl} d\varepsilon_{kl} \tag{25}$$

with the elastoplastic stiffness tensor:

$$\Lambda_{ijkl} = K\delta_{ij}\delta_{kl} + 2G\left(\delta_{ik}\delta_{jl} - \frac{1}{3}\delta_{ij}\delta_{kl}\right) - h(L)\left(2Gn_{ij} + \sqrt{\frac{2}{3}}KD\delta_{ij}\right)\Pi_{kl} \tag{26}$$

where $h(L)$ is the Heaviside step function, with $h(L) = 1$ for $L > 0$ and $h(L) = 0$ for $L \leq 0$.

3. Model validation and numerical model

Following the procedure provided by Liao et al. (2021), the J_2 model is implemented with the adoption of the substepping scheme with error control (Sloan and Booker, 2010). Subsequently, this section presents the validation of the MPM procedure coupled with the J_2-model and the MPM modeling for pipe-soil interaction.

3.1. Model validation using element tests

The element tests of triaxial compression were conducted to validate the implemented J_2 model and calibrate the model parameters of the Stockton Beach Sand (STK), which were used in the simulations of pipe-soil interaction. The mean diameter d_{50} of STK sand is 0.4 mm, and the maximum and minimum void ratios are 0.778 and 0.497, respectively. Several element tests of STK sand with different initial void ratios e_0 were carried out under two initial confining pressures p_0 (e_0 = 0.551, 0.64 and 0.72 for $p_0 = 150$ kPa; $e_0 = 0.574$, 0.64 and 0.72 for $p_0 = 500$ kPa). The size of the element was modeled as 1 m × 1 m × 1 m, where 2 material points were set in each direction (i.e. a total of 8 material points). The confining pressure of the specimen was imposed by the nodal load exerted on the lateral surface of the element, and the prescribed nodal velocity was applied downward at the top surface to simulate the strain-driven triaxial compression.

Following the calibration procedure of Yang et al. (2019), the determined model parameters of STK sand are listed in Table 1. A straight line in the e-ln$p$' space is adopted to describe the critical state line for STK sand (Ajalloeian et al., 1996), in which the values of e_Γ and λ_c are taken as 0.925 and 0.037, respectively. The critical stress ratio M_c at triaxial compression is set to 1.23, which was verified by triaxial compression tests (Ajalloeian et al., 1996), and the value of c is estimated to be 0.75 due to the lack of triaxial extension data.

Fig. 2 presents the simulated results of triaxial compression and available test data from Ajalloeian et al. (1996). The dense sand generally shows a satisfactory stress–strain curve under different confining pressures, although the stress response under p_0 = 150 kPa is somewhat underestimated. For the loose sand, its strain-hardening and contractive behaviors are also revealed. In addition, the state-dependent model well captures the more significant dilative response of sand samples for lower confining pressures and higher relative densities.

Table 1
Parameters of the J_2-deformation type model for STK sand.

Elastic parameters	Critical state parameters	Dilatancy parameters	Softening parameter
$G_0 = 250$ $\kappa = 0.012$	$M_c = 1.24$ $c = 0.75$ $e_\Gamma = 0.925$ $\lambda_c = 0.037$	$d_0 = 0.45$ $m = 4.1$	$\varepsilon_r = 0.06$

3.2. Biaxial compression tests

To further examine the applicability and mesh sensitivity of the J_2 model in the typical boundary value problem, the MPM models were applied to simulate the biaxial compression tests under plane strain conditions. The schematic model setup is illustrated in Fig. 3. First, the dense sand specimen with $e_0 = 0.581$ is consolidated homogeneously under a confining pressure of 400 kPa. Then, a vertical downward velocity of 0.03 m/s is applied to the rough rigid plate on the top of the specimen to perform axial compression. The rigid plate-specimen interaction is characterized by the rigid contact algorithm mentioned above. During the compression process, a fixed constraint is imposed on the bottom boundary, and a constant confining pressure is applied to the lateral boundaries through the particle load. As shown in Fig. 3, the analysis also compares four combined cases (i.e. C4, M4, M9 and F4) with different mesh sizes (C: coarse mesh of 0.125 m, M: medium mesh of 0.1 m and F: fine mesh of 0.0625 m) and various numbers (4 and 9) of particles per element (NPPE). The same material parameters in Table 1 are employed for the simulation. Gravity is not considered in the biaxial compression tests.

Fig. 4 presents the global stress–strain relationship of the four cases, in which the vertical stress indicates the contact force per unit area acting on the rigid plate and the axial strain is obtained by dividing the vertical displacement of the loading plate by the initial height of the specimen. Evidently, the tests with different mesh sizes or NPPEs show a basically consistent response. However, finer meshes or more NPPEs appear to predict higher peak stress and smaller peak strain. For the three tests (C4, M4 and F4) with identical NPPEs, the finer mesh tests generally reflect a more significant softening response after the peak value. The predicted steady-state stresses are close in these three cases. Compared with the M4 case, M9 with more NPPEs renders a relatively weak softening response and mildly higher steady-state stress. A larger number of particles per element is beneficial to reducing the integration error (Steffen et al., 2008); however, the increasing computational cost should also be taken into account. It is noted that the mesh dependency issue can be resolved by invoking regularization techniques (Bažant et al., 1984; Mallikarachchi and Soga, 2020), which are not discussed here and will be left for future study. The differences in the mechanical response for the four cases are considered insignificant.

Fig. 5 further compares the deviatoric strain and void ratio distribution of the four different samples at axial strain ε_a = 15%. The two symmetric shear bands in the sample can be easily identified by concentrated large strains and prominent dilatancy, while the domain outside the shear bands is approximately elastically loaded with smaller volumetric strain. Fig. 5a exhibits that the shear bands predicted in the sample are narrower for the finer mesh test. Moreover, the bandwidth appears to be more sensitive to the mesh size than NPPE, which is consistent with the coupled MPM/DEM simulations in the study of Liang and Zhao (2019).

Two material points Pt.1 and Pt.2 (their positions are marked in Fig. 5a) inside sample F4 were selected to further analyze the local responses. As seen from Fig. 6, prior to the axial strain reaching 1.3%, the evolutions of the deviatoric stress or volumetric strain of the two points are in general agreement, indicating that the specimen deforms homogeneously with initial volumetric contraction. As the loading continues, the stress response of Pt.2 first shows post-peak softening because of the accumulation of deviatoric strain and strain localization. Subsequently, the stress state of Pt.1 also experiences certain unloading. However, due to the formation of shear bands and the constraints of the rough boundary, the stresses at Pt.1 immediately undergo an increase and then remain at a relatively high level. During this process, Pt.2 located in the shear bands undergoes prominent dilatancy and finally reaches the

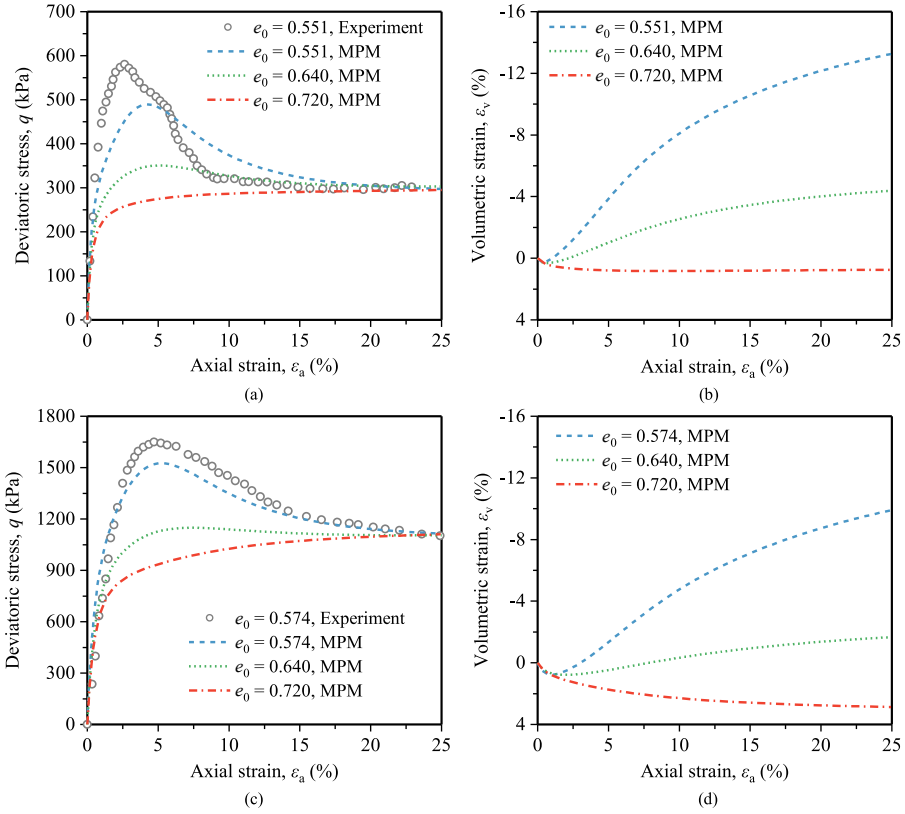

Fig. 2. Comparison between MPM simulations and available test results of triaxial compression for STK sand: (a) Stress–strain curves under p_0 = 150 kPa; (b) Volumetric-axial strain curves under p_0 = 150 kPa; (c) Stress–strain curves under p_0 = 500 kPa; and (d) Volumetric-axial strain curves under p_0 = 500 kPa.

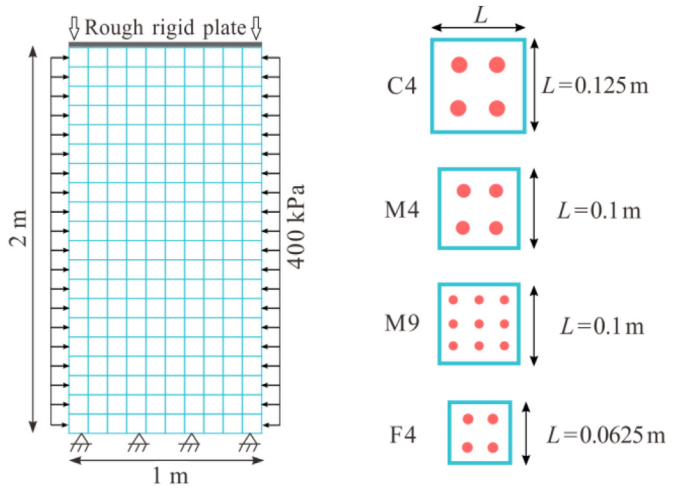

Fig. 3. Schematic of the MPM model for biaxial compression tests with various mesh sizes and NPPEs.

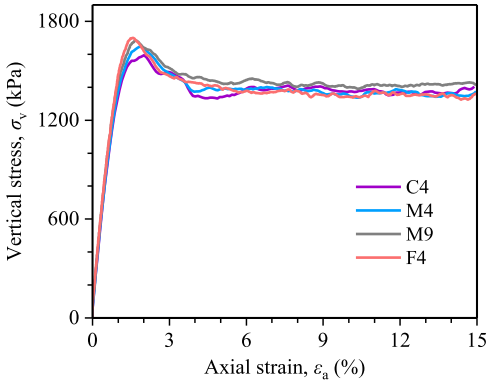

Fig. 4. Comparison of the global stress–strain responses for biaxial compression tests with different mesh sizes and NPPEs.

critical void ratio, while Pt.1 far away from the shear bands only experiences a relatively slight volume change.

3.3. MPM modeling

The plane strain MPM model for the simulation of pipe-soil interaction is shown in Fig. 7. Considering the vertical symmetry of the geometry and computational efficiency, only half of the analysis domain is modeled. The background mesh is composed of structured square elements. Each element contains 4 material points in the initial configuration, except for the quadrilateral zone with a dense arrangement of particles near the pipe.

The buried pipe is modeled as a rigid cylinder with a diameter D. The rigid contact algorithm is employed to handle the frictional contact between the soil and the pile. The interfacial friction coefficient μ is usually determined through the expression $\mu = \tan\delta$ and the definition of the interface friction angle δ, which comprehensively reflects the roughness of the pipe surface and the characteristics of the soil. For pipe surfaces with different rust levels and coatings, δ usually lies between 20° and the friction angle φ of the soil (Durgunoglu and Mitchell, 1973; Yimsiri et al., 2004). In the

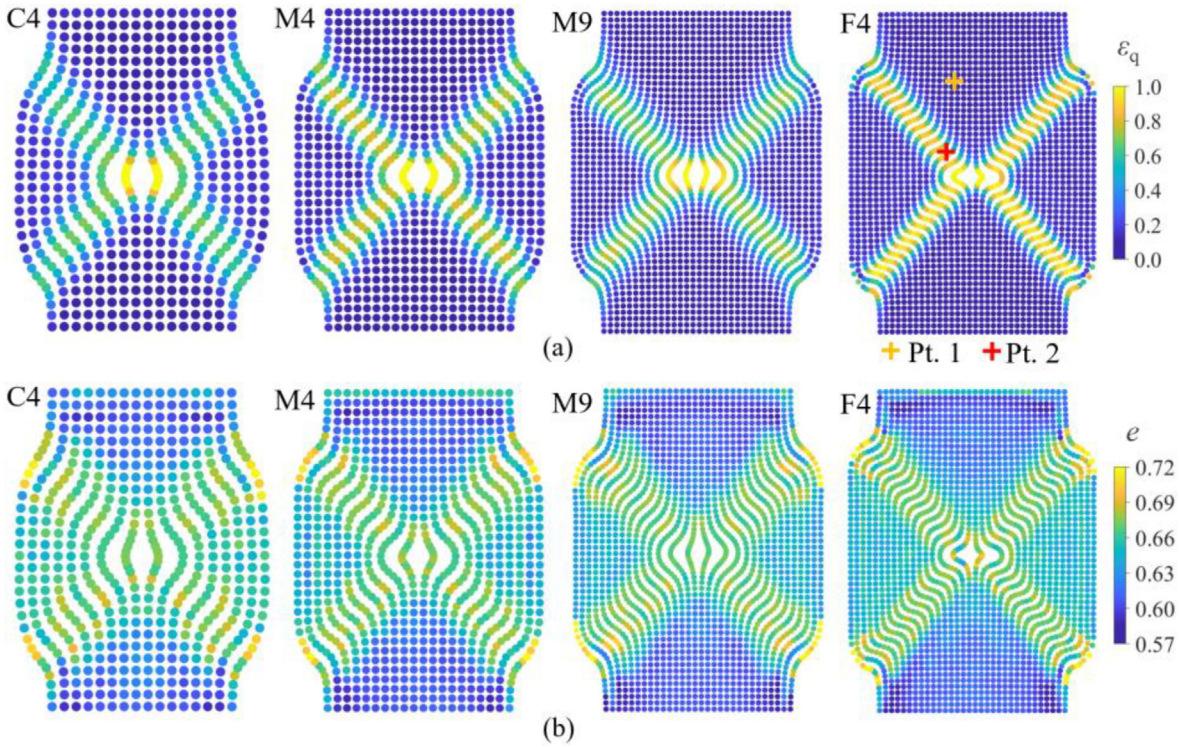

Fig. 5. Contour of (a) Deviatoric strain and (b) Void ratio of samples for the four cases (C4, M4, M9 and F4) at the final state $\varepsilon_a = 15\%$.

pipe-soil interaction simulation, the value of δ typically ranges from 0.5φ to 0.6φ (Jung et al., 2016; Ni et al., 2018; Qin et al., 2019). Some parameter studies based on theoretical analysis (White et al., 2008) and numerical simulations (Yimsiri et al., 2004; Jung et al., 2016) indicated that there is no obvious variation in resistance response when the value of u varies within this range. For the present MPM modeling, the interface friction angle δ is reasonably assumed to be $0.6\varphi_c$ (φ_c is the critical state friction angle of the soil and is calculated from the critical stress ratio M_c).

The distance between the pipe and the side boundary is selected as $14D$ based on the numerical study and the experimental results (Limnaiou et al., 2019; Wu et al., 2021), which is a sufficiently large distance to eliminate the boundary effect. The burial depth H (i.e. the distance from the soil surface to the pipe springline) of the pipe is determined by the embedment ratio H/D. From the numerical results conducted by Limnaiou et al. (2019), it can be deduced that the determination of the bottom boundary location is generally related to the burial depth. On the premise of effectively avoiding boundary effects and reducing computational costs, the soil medium under the pipe is adjusted at depths of $(6–10)D$ with different H/D conditions. The two lateral side boundaries are fixed in the normal direction, whereas the bottom boundary is fully fixed in both the horizontal and vertical directions.

Before applying any motion to the pipe, the geostatic stress loaded by gravity is obtained with the introduction of local damping (Bhandari et al., 2016; Zhang et al., 2022). Afterwards, the specified vertical downward velocity is imposed on the rigid pipe without numerical damping. During this simulation, a cohesion of 1 kPa is considered for the soil model to prevent the generation of tensile stress and promote numerical stability, which is implemented by adding the equivalent cohesion to the normal stress following Liao et al. (2021). In the explicit MPM scheme, the critical time step is reduced by multiplying the Courant number of 0.3 to ensure solution stability.

4. MPM results and parametric study

4.1. MPM results for model tests

The MPM model is further validated against the experimental results by Wu et al. (2021) for vertical penetration of rigid pipes buried in STK sand. Wu et al. (2021) pulled the pipe section downward with a maximum displacement of $0.75D$. In the physical model tests, different burial conditions, including the relative density ($D_r = 19\%–92\%$) of sand and embedment ratio ($H/D = 1.5–4$), were considered. The thickness and material of the pipe allow its negligible deflection and ovalization during pipe penetration, which ensures the rigid behavior of the pipe and the plane strain of the setup. The friction force developing at the chamber sidewall-pipe interface and the cable-pulley system was specifically measured and subtracted from the reaction measured by the load cell to obtain the net reaction force acting on the pipe.

The pipe is modeled with the same diameter ($D = 37.5$ mm) as the experiments. Since the sand around the pipe is often in a medium-to-dense state under practical conditions, only medium and dense sands with initial void ratios $e_0 = 0.657$ and 0.524 are tested in the simulation, which are consistent with the compactness of sands used in the model tests (Wu et al., 2021). For a more detailed comparison with the experiment, the MPM model is performed with an embedment ratio of 3. A fine mesh of grid size 4.6875 mm × 4.6875 mm is chosen to better capture the evolution and thickness of the shear bands after checking the mesh size effect. The values of other input parameters for the J_2-model are consistent with those in Table 1, and these calibrated model parameters are used for sands of any relative density and stress level. Moreover, the specified downward velocity of the pipe is set to 4 mm/s after examining the effect of loading rates, which is much higher than that in the model tests. Because the strain-rate dependence is not considered in the soil constitutive model, the

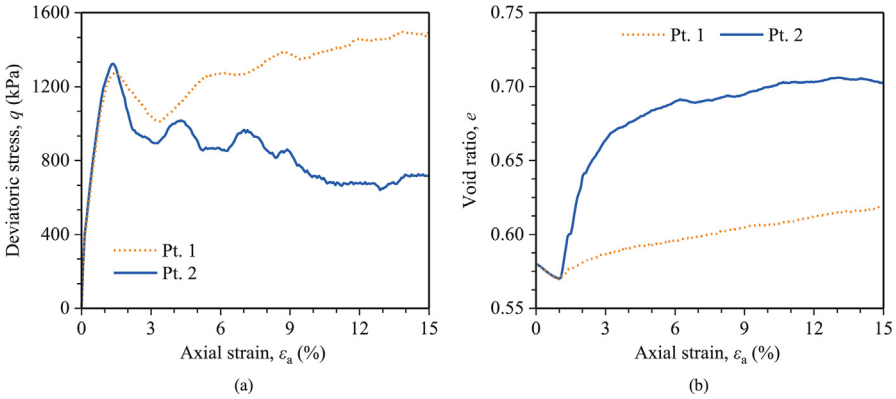

Fig. 6. Evolution of (a) Deviatoric stress and (b) Void ratio at the selected material points in the F4 case.

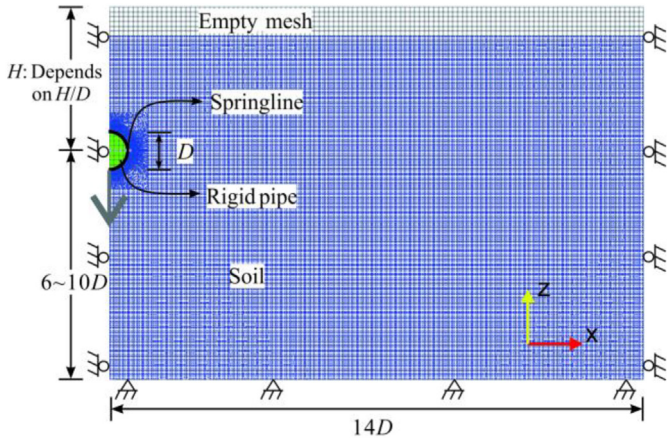

Fig. 7. MPM model of pipe-soil interaction for downward pipe movement.

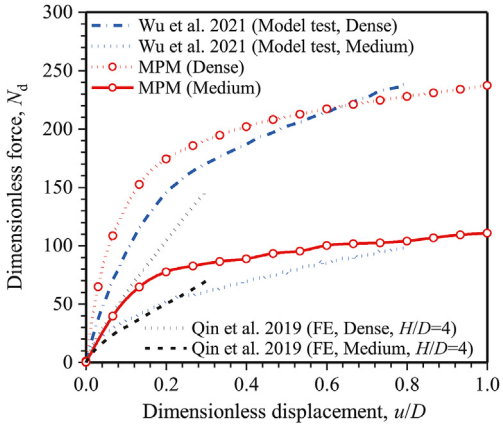

Fig. 8. Comparison of force–displacement curves from MPM simulations and model tests at $H/D = 3$.

velocity has little influence on the reaction exerted on the pipe under the condition of insignificant dynamic effects.

Fig. 8 displays the simulated and experimental force–displacement curves, which are expressed in the form of dimensionless force $N_d = F/\gamma HD$ versus dimensionless displacement u/D, where F is the soil reaction force acting on the pipe, γ is the unit weight of soil calculated from the initial void ratio e_0 and the specific gravity $G_s = 2.65$ of STK sand, and u is the vertical downward displacement of the pipe. For the pipe buried in dense sand, the results from the MPM simulations are in good agreement with the experimental data (Wu et al., 2021), as depicted in Fig. 8. The reaction force initially increases in a nonlinear stage and then increases approximately linearly with the penetration of the pipe. The simulated results show a slightly flatter slope in the linear ascending phase. As illustrated in Fig. 9, the reaction force acting on the pipe at the transition of the force–displacement curve from nonlinear to steady-state is defined as the failure threshold Q_{df}, and the downward displacement corresponding to Q_{df} is denoted as u_{df}, which are two important parameters for the design of buried pipelines. Following the approach used by Qin et al. (2019) and Wu et al. (2021), the transition point is determined as the intersection between the descending segment and the stable segment of the slope curve $\Delta N_d/(\Delta u/D)$–u/D, where $\Delta N_d/(\Delta u/D)$ tends to change slightly with u/D.

The soil density significantly influences the dimensionless force curves. The pipe in the medium sand mobilizes the considerably smaller soil resistance during the downward movement. The MPM results give an overall overprediction of the dimensionless force N_d for medium sand, which is reflected in the stiffer initial response and lower steady ascending rate. This difference may be due to the overestimation of the interfacial friction coefficient for medium sand, in which a fixed value is adopted for different soil densities. The rougher friction boundary restricts the relative movement between the pipe and the soil, and in turn, affects the mobilization of soil resistance. Moreover, the initial geostatic stress distribution generated by gravity loading in the simulation is theoretically linear with depth, whereas an approximate parabolic distribution lower than the theoretical values is measured in the tests due to the sand-sidewall friction (Ansari et al., 2018; Wu et al., 2021).

Qin et al. (2019) also conducted FE modeling to test the resistance response of the pipe within the $0.3D$ penetration depth under different burial depths, in which the pipe diameter was 102 mm and the soil was modeled using the Mohr–Coulomb model. The FE results with embedment ratio $H/D = 4$ are selected for comparison due to the lack of a simulation for $H/D = 3$. Some discrepancies between the FE results and MPM or experimental results are shown in Fig. 8, which could be partly attributed to the difference in constitutive models and parameters. In the FE model of Qin et al. (2019), the friction angle and dilation angle of sand are constant for a particular initial density, and the elastic modulus is determined according to the initial stress at the pipe springline and the relationship proposed by Janbu (1963). This is obviously insufficient to characterize the actual strength and the stiffness response of the soil due to the significant changes in the stress level and soil density during the downward movement of the pipe. It should also be mentioned that Qin et al. (2019) identified the failure threshold

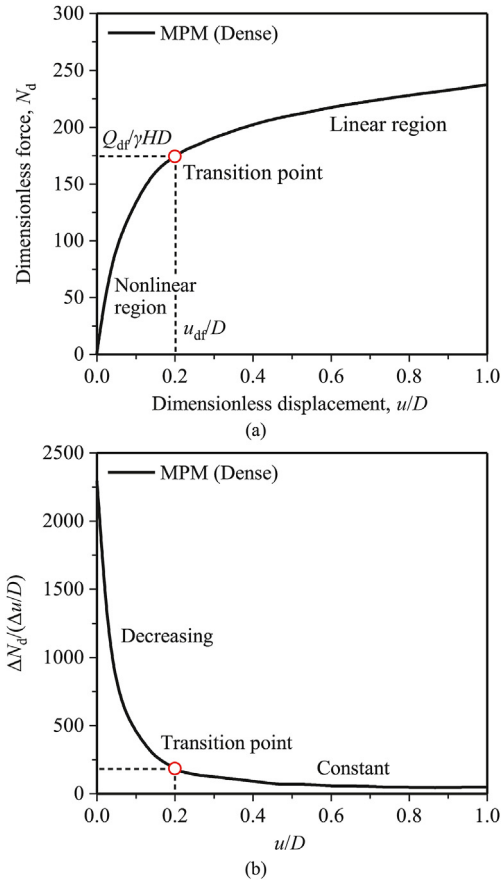

Fig. 9. Method for determining the failure threshold Q_{df} and the associated pipe displacement u_{df}: (a) N_d–u/D curve and (b) $\Delta N_d/(\Delta u/D)$–u/D curve for dense sand under $H/D = 3$.

within the displacement of 0.1D, after which a linear ascending pattern of N_d was predicted. The inaccurate prediction would cause an evident underestimation of the failure threshold. On the whole, the MPM framework coupled with the J_2-model can reasonably predict the resistance response developing on the pipe with downward movement.

To further explain the evolution of the resistance exerted on the pipe with increasing penetration depth, the failure mechanism developing in the sand needs to be investigated. The deviatoric strain contours corresponding to three typical pipe displacements of dense sand and medium sand are illustrated in Fig. 10. In the initial nonlinear stage ($u/D = 0.06$) of the resistance response, a triangular soil wedge is formed beneath the pipe. As the pipe moves to near the depth corresponding to the failure threshold ($u/D = 0.2$), the log-spiral wedge is mobilized, and the shear band above the pipe gradually develops from the springline to the soil surface. The same failure pattern was also observed in model tests (Wu et al., 2021) and other numerical results (Kouretzis et al., 2014). With the continuous penetration of the pipe ($u/D = 0.9$), the geometry of the shear bands remains basically unchanged. The soil wedge below the pipe is pushed downward with shear bands extending to the surface. Meanwhile, the deviatoric strain concentration zone as a part of the log-spiral shear band is consistently moved downward, and the shear band is continuously enhanced and widened. The pipe penetration over a greater depth may neutralize the softening of the soil and reduce the brittle response to some extent. As has been pointed out by White et al. (2008), this steady ascending resistance response is tightly associated with a combination of soil softening and continuous expansion of the shear bands at depths. The failure mechanism is of course related to the stress level and burial condition, which will be discussed in the following section.

As shown in Fig. 10, the dense sand deforms with a larger size of the soil wedge and more significant surface heave than the medium sand, owing to the stronger dilatancy behavior of the dense sand. In addition, the soil above the pipe has not completely collapsed, which may be associated with the lower stress level under the small diameter pipe and the cohesion added to the model. The contribution of the weight of the soil wedge above the pipe to the resistance is approximately γHD (i.e. 1 of dimensionless force N_d), the influence of which on the force–displacement curve is negligible.

Fig. 11 shows the displacement contours of the surrounding soil as the failure threshold is mobilized. The soil deformation field can be characterized by the combined patterns extracted by Ganju et al. (2021), in which the influence zone is divided into a triangular

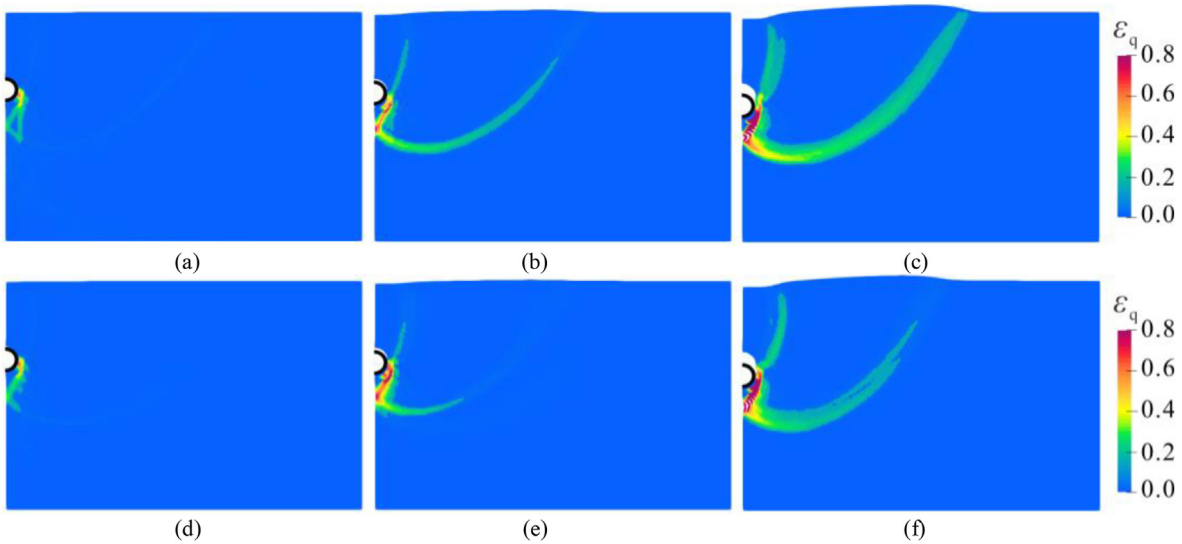

Fig. 10. Deviatoric strain contours during the downward movement of pipe under $H/D = 3$ for dense sand at (a) $u/D = 0.06$; (b) $u/D = 0.2$; (c) $u/D = 0.9$; and for medium sand at (d) $u/D = 0.06$; (e) $u/D = 0.2$; (f) $u/D = 0.9$.

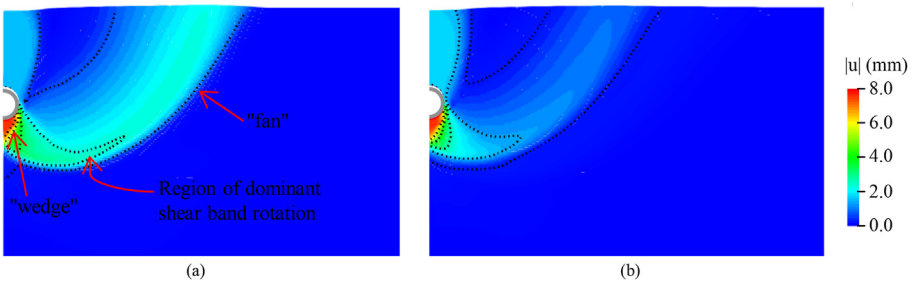

Fig. 11. Displacement contours developing in (a) Dense sand and (b) Medium sand corresponding to the mobilization of the failure threshold.

wedge below the pipe, a fan zone, and a transition zone between the wedge and the fan. Larger transition zones mobilized by the triangular wedge are observed in dense sand, and the displacement contours in the fan zone stretch to the ground surface (Fig. 11a). Even though non-uniform displacements tend to form in the fan with the continuous penetration of the pipe, this deformation pattern is very similar to the rigid-plastic response observed in dense sand (Wu et al., 2021). A relatively small influence zone is mobilized in medium sand (Fig. 11b), which is closely related to the densification process and weaker dilatancy of the sand.

4.2. Effect of pipe diameter

A large number of experimental and numerical results have revealed that the resistance exerted on the structure and the displacement field of the surrounding soil during the soil-structure interaction are affected by various factors, such as the geometry and size of the structure, the stress level and the relative density of the soil (Zhu et al., 2001; Guo and Stolle, 2005; White et al., 2008; Kouretzis et al., 2014; Ganju et al., 2021). Next, comprehensive parametric analyses were performed to investigate the effects of the pipe diameters and burial depths. The sands with the above two initial void ratios (e_0 = 0.657 and 0.524 for medium and dense sands, respectively) are considered, and the model parameters are kept consistent with those in the above simulations of the model tests. Since the resistance response is relatively insensitive to the mesh size, the following meshing rules are formulated: the mesh size under different pipe diameters D is set to $1/8D$ and does not change with the burial depth.

The MPM simulations were conducted with various pipe diameters under H/D = 3. The dimensionless force–displacement curves of three different pipe diameters for dense sand and medium sand are illustrated in Fig. 12a and b, respectively. The larger diameter leads to higher confining pressure around the pipe and thereby less dilatancy according to the state-dependent dilatancy function D in Eq. (17). For this reason, the smaller reaction force is mobilized under the same dimensionless displacement u/D for a relatively large diameter. The dimensionless failure threshold N_{df} (i.e. $Q_{df}/\gamma HD$) decreases, and the corresponding downward displacement u_{df}/D increases with the pipe diameter. The same trend of resistance response associated with this scale effect was also observed in the lateral and vertical downward movement of the pipe (Guo and Stolle, 2005; Jung et al., 2016).

The dimensionless displacement u_{df}/D corresponding to N_{df} ranges from 0.2 to 0.32 for various pipe diameters in dense sand, and 0.22–0.29 for medium sand. The simulated u_{df}/D is significantly higher than 0.05–0.08 obtained from FE results (Qin et al., 2019). Actually, Qin et al. (2019) determined the failure threshold Q_{df} based completely on the shape of the force–displacement curve within the downward movement of $0.3D$, without the combination with the complete failure mode. This evaluation method in the case of insufficient pipeline displacement can easily cause an underestimation of the failure threshold and the mobilization displacement.

Fig. 13 shows the contours of the deviatoric strain of the surrounding soil at $u = 0.9D$, which are selected from the steady ascending stage of resistance to capture the complete failure pattern. At this time, the shear band above the pipe stemming from the springline curves mildly inwards and extends to the soil surface, and the log-spiral shear band is gradually widened or multiple shear bands are mobilized due to the continuous penetration of the triangular failure wedge. Wu et al. (2021) observed the same failure mechanism in physical experiments, including the collapsed wedge and the log-spiral wedge. Compared with the simulated results of the smaller pipe diameter in Fig. 10, it can be found that as the pipe diameter increases, the collapsed wedge above the pipe deforms more significantly, and the log-spiral shear bands become more

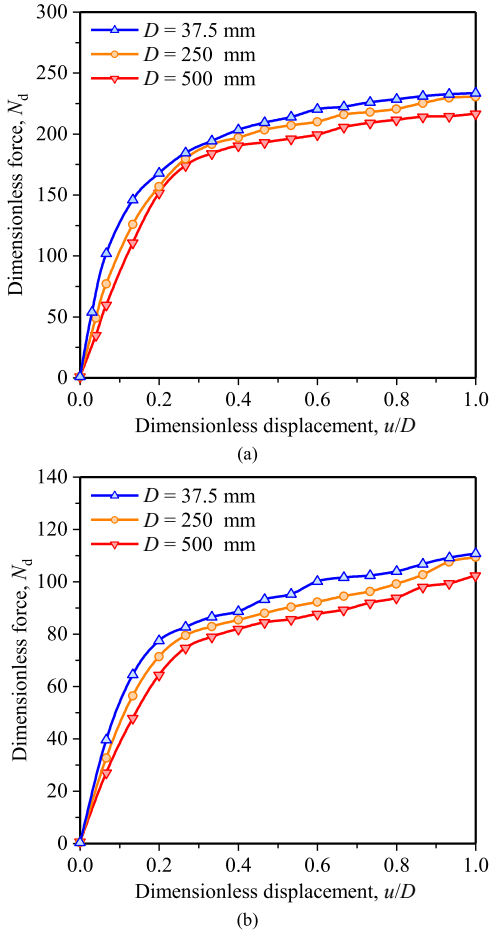

Fig. 12. Effect of pipe diameter D on the force–displacement curve under H/D = 3 for (a) Dense sand and (b) Medium sand.

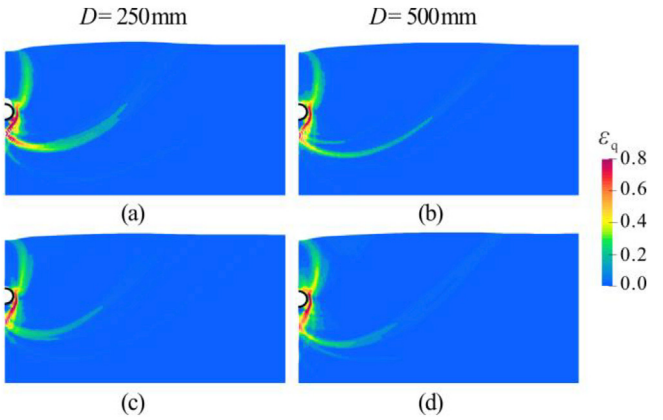

Fig. 13. Deviatoric strain contours developing in (a–b) Dense sand and (c–d) Medium sand with different pipe diameters at $u = 0.9D$.

difficult to extend to the surface. In contrast to the general shear failure mode developing in dense sand, the high deviatoric strain zone in medium sand is confined not far from the triangular failure wedge, and the log-spiral shear band is more localized (Fig. 12). Therefore, the failure mode in the medium sand is closer to the local shear failure mode.

The simulated failure surfaces and the relative analytical slip surfaces are plotted in Fig. 14. Since the failure surfaces associated with bearing capacity can hardly extend to the ground surface, only the triangular active zone and the transition zone surrounded by the log-spiral surface in the general shear failure mode for strip footing are plotted for comparison. If the pipe diameter is equivalent to the footing width and the pipe springline is assumed to be the bottom corner of the footing, the log-spiral slip surfaces in Prandtl's solution can be described through $r = r_0 e^{\psi \tan\varphi}$. In this equation, r is the length from the springline to any point on the slip surface, r_0 is the length of the side boundary of the triangular wedge and is calculated by the angle $45° + \varphi/2$ between this line and the horizontal direction, and ψ is the rotation angle from r_0 to r. For both dense and medium sand, the simulated slip surfaces with various pipe diameters are in good accordance with the analytical prediction over a specific range of the friction angle φ. The location of the slip surfaces caused by bearing capacity failure is basically consistent with that captured in the model tests (Wu et al., 2021). Moreover, deeper failure surfaces with a shorter extension are captured due to the higher stress levels for relatively large pipes.

4.3. Effect of burial depth

A series of simulations for different H/D values ($H/D = 2–8$) with the same pipe diameter (D = 500 mm) were conducted to investigate the influence of burial depths on the resistance response and failure mode of the surrounding soil. Fig. 15a and b presents the simulated force–displacement curves for dense and medium sand, respectively. Several observations and features of the N_d–u/D curves are outlined as follows: (1) the overall level of the dimensionless reaction force within the downward pipe displacement of $1D$ descends with increasing burial depth; (2) the dimensionless failure threshold N_{df} reduces with increasing H/D, and the burial condition of dense sand shows a more significant reduction of N_{df} compared to that of medium sand; and (3) a larger dimensionless displacement u_{df}/D is needed to mobilize N_{df} under higher H/D values.

Likewise, the simulated deviatoric strain contours of the three typical stages (the nonlinear ascending stage of resistance, near the failure threshold and the steady ascending stage) for dense sand and medium sand are presented in Figs. 16 and 17, respectively, which illustrate the different evolution patterns of shear bands for different H/D ratios. For clarity, only the strain development regions near the pipe are plotted under $H/D = 6$, instead of the entire area reaching the surface. As depicted in the first column of Figs. 16 and 17, at the beginning of pipe penetration, there are also two prominent shear bands developing in dense and medium sand under $H/D = 2–6$, one (f_1) surrounding the triangular soil wedge and the other (f_2) developing vertically downward from the pipe springline. Compared with medium sand, a larger triangular compression wedge beneath the pipe is formed in dense sand under the same H/D, as observed in model tests (Wu et al., 2021). Additionally, the size of the triangular wedge in the dense sand shows a significant decrease with burial depth, which may be because the overall higher dilatancy response in dense sand is more susceptible to the initial stress level. For the deeply buried condition ($H/D = 6$), a relatively large pipe displacement is required to reach the failure threshold. During this penetration process, several small shear bands develop with changes in the soil wedge size.

At u_{df} (second column of Figs. 16 and 17), the formation of the complete failure mechanism is accompanied by the extension of the slip surface f_3 originating from the bottom of the triangular wedge. For $H/D = 6$, several similar slip surfaces of different sizes gradually form (Figs. 16h and 17h), instead of the shear band f_3 with the concentrated deviatoric strain under shallower burials. Meanwhile, shear zone f_4 develops from the springline to the ground surface for $H/D = 2$ and 4, whereas a diffused strain zone forms above the pipe for $H/D = 6$. This might be expected because, in the case of deep burial, the surrounding soil primarily infills the cavity above the pipe, making it more difficult to form the overall soil instability.

At larger penetration depths (third column of Figs. 16 and 17), the shear bands are further widened with higher deviatoric strain

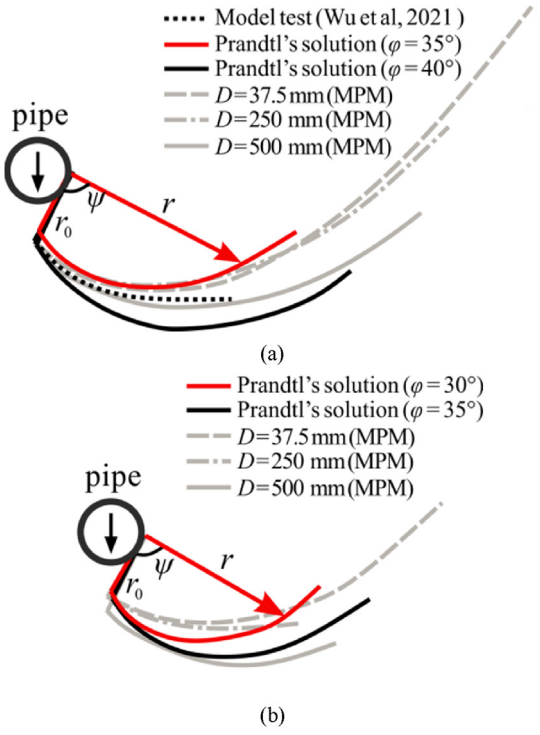

Fig. 14. Comparison of failure surfaces induced by bearing capacity from MPM simulations and analytical solutions for (a) Dense sand and (b) Medium sand.

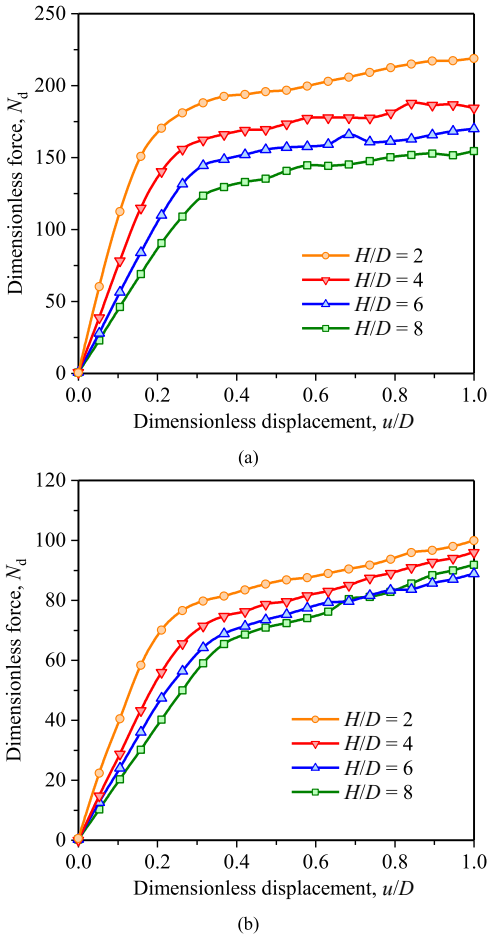

Fig. 15. Effect of embedment ratio H/D on the force–displacement curves with $D = 500$ mm for (a) Dense sand and (b) Medium sand.

concentrations. However, for the dense foundation with $H/D = 6$ (Fig. 16i), a new f_3-type failure surface forms from the edge of a larger soil wedge, surrounded by shear bands that develop downward from the pipe springline and curve inwards. Qin et al. (2019) also captured homologous shear bands that propagate deeply into the ground. Although more small shear bands are mobilized with pipe penetration under $H/D = 6$, it is worth noting that the high strain zones are mainly concentrated near the pipe. Moreover, the range of shear bands in dense sand is wider and deeper than that in medium sand due to the more significant dilatancy of the soil. The simulated failure pattern for $H/D = 8$ is almost identical to that for $H/D = 6$ and thus is not presented here.

4.4. Prediction of bearing capacity under different burial depths

The estimation of the failure threshold Q_{df} and the corresponding pipe displacement u_{df} controls the response of the vertical bearing spring for modeling the pipe-soil interaction with the nonlinear Winkler soil spring model (ALA, 2005; Kouretzis et al., 2015). Following the approach of Qin et al. (2019) and Wu et al. (2021), Q_{df} is determined from the force–displacement curve of $D = 500$ mm, which is closer to the practical pipe diameter. The results are plotted in Fig. 18. For comparison, Fig. 18 also summarizes the results calculated from the physical model tests (Wu et al., 2021), FE modeling (Jung et al., 2016; Qin et al., 2019), FELA (Kouretzis et al., 2014) and current design guidelines (ALA, 2005). ALA (2005) adopts the classic bearing capacity equation to estimate the ultimate vertical force acting on the pipe, which can be expressed as

$$Q_{df} = N_c cD + N_q \gamma HD + N_\gamma \gamma D^2/2 \tag{27}$$

where c is the cohesion, and N_c, N_q and N_γ are the bearing factors. The first term on the right-hand side is assumed to be zero for dry cohesionless sand. N_q and N_γ are calculated based on:

$$N_q = e^{\pi \tan\varphi} \tan^2(45^\circ + \varphi/2) \tag{28}$$

$$N_\gamma = e^{(0.18\varphi - 2.5)} \tag{29}$$

For dense sand, the MPM results show good agreement with the analytically calculated values given by ALA (2005) within the investigated embedment ratios, which indicates a reduction in N_{df} with increasing burial depth, especially for $H/D < 3$. Comparatively, the FEM results present considerable underestimations, which may be attributed to the positioning deviation of the failure threshold in the case of insufficient pipe penetration depth. For Qin et al. (2019) and Jung et al. (2016), the failure thresholds under different burial depths were determined at pipe displacements u_{df} of $(0.05–0.08)D$ and $(0.057–0.062)D$, respectively, which were relatively small compared with the MPM results and the experimental results of Wu et al. (2021). Moreover, the difference between the MPM-calculated values and the experimental results is associated with the scale effects discussed above.

As illustrated in Fig. 18b, under the medium sand condition, the numerical results from the present MPM analysis are higher than the bearing capacity calculated from the ALA (2005) guideline with the representative medium sand friction angle $\varphi = 36^\circ$. Instead, the MPM results are generally close to the values calculated with a higher friction angle $\varphi = 39^\circ$. The results from the experiments (Wu et al., 2021) and the FELA analysis using $\varphi = 36^\circ$ (Kouretzis et al., 2014) are further compared with the MPM data, which reveals that the MPM-simulated results in the medium sand may be overestimated to a certain extent. Practically, this overestimation has been noticed in the calibration with the model tests. It is noteworthy that the representative values of the friction angle for dense and medium sand are both smaller than the peak friction angle measured from direct shear tests corresponding to the stress level at the pipe springline. As pointed out by Wu et al. (2021), the equivalent friction angle obtained following the approach proposed by Davis (1968) is more appropriate for estimating the failure threshold with the ALA guideline. Overall, the MPM results could provide some reference for reasonable estimates of Q_{df} and evaluate the efficacy of the ALA guideline for predicting the bearing capacity.

The simulated mobilization displacement u_{df}/D associated with Q_{df} for various burial depths and sand densities is plotted in Fig. 19. The simulation results show that the dimensionless pipe displacement u_{df}/D increases approximately linearly with the embedment ratio H/D for different sand densities, while the experimental data (Wu et al., 2021) indicate that u_{df}/D is not insensitive to H/D with a relatively small diameter pipe. In addition, the pipe displacement required to mobilize the failure threshold in medium sand is slightly higher than that in dense sand, unlike the results obtained from model tests (Wu et al., 2021). The simulated pipe displacement u_{df} ranges from $0.25D$ to $0.35D$ for $H \leq 8$ under both dense and medium sand conditions and is significantly higher than the mobilization displacement of $0.1D$ recommended by the ALA (2005) and $(0.05–0.08)D$ obtained from FE modeling (Qin et al., 2019). Given the form of force–displacement curves and the constant value of Q_{df}, a relatively low displacement u_{df} will lead to overestimating the reaction force developing on the pipe. Therefore, according to the MPM

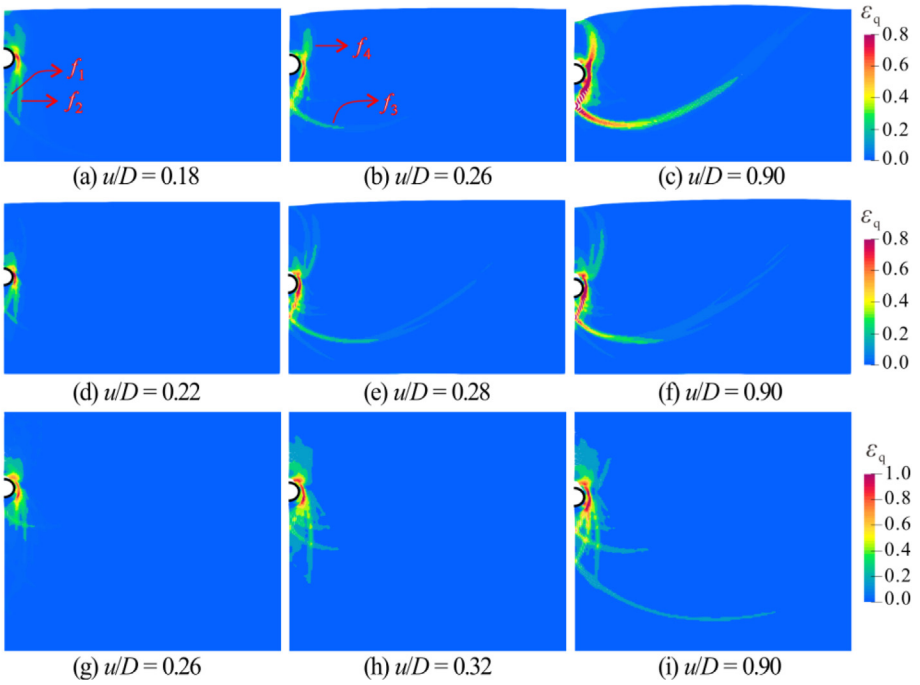

Fig. 16. Deviatoric strain contours during pipe penetration for dense sand under (a–c) $H/D = 2$; (d–f) $H/D = 4$ and (g–i) $H/D = 6$.

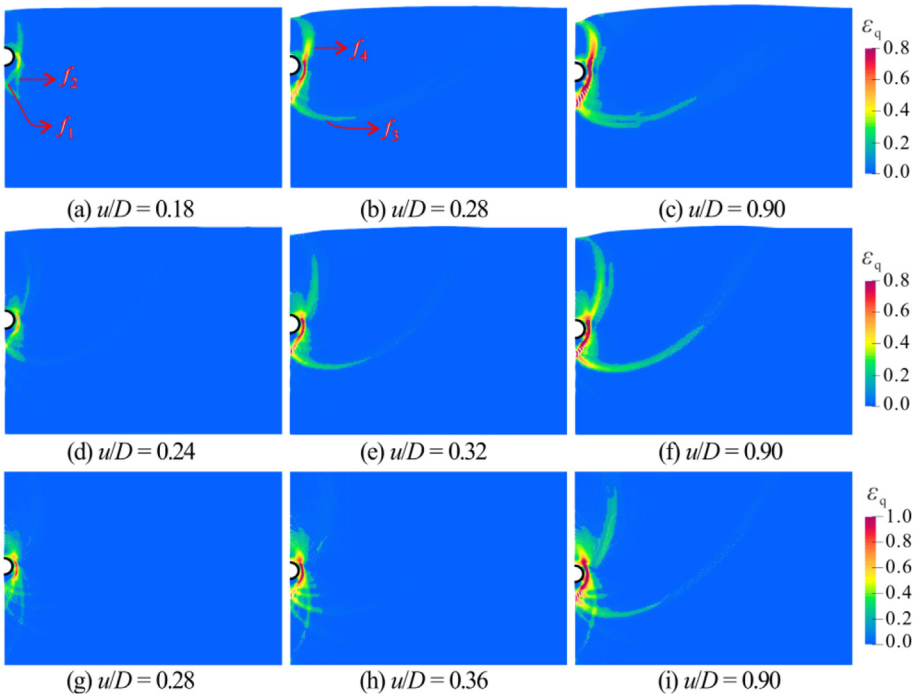

Fig. 17. Deviatoric strain contours during pipe penetration for medium sand under (a–c) $H/D = 2$; (d–f) $H/D = 4$ and (g–i) $H/D = 6$.

results, it may be more appropriate to choose a mobilization displacement of 0.3D when elastoplastic soil springs are used to analyze the pipe stress and deformation.

5. Conclusions

The BSMPM is adopted to investigate the evolution of the reaction force on the pipe and the failure mechanism of the surrounding soil during rigid pipe penetration. The stress–strain behavior of soil is modeled using the J_2-deformation type model with state-dependent dilatancy proposed by Yang et al. (2019), which can accurately capture the soil response under varying relative density and stress levels. The reliability and accuracy of the MPM modeling are validated through comparison with published scaled physical model tests of bearing capacity for buried pipes. The influences of pipe diameter and burial depth on the bearing

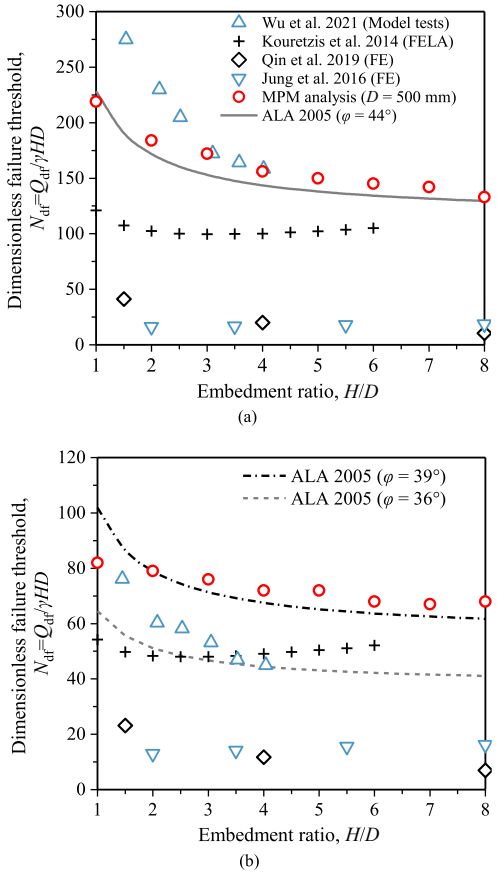

Fig. 18. Comparison of normalized failure bearing capacity versus embedment ratio for (a) dense sand and (b) medium sand.

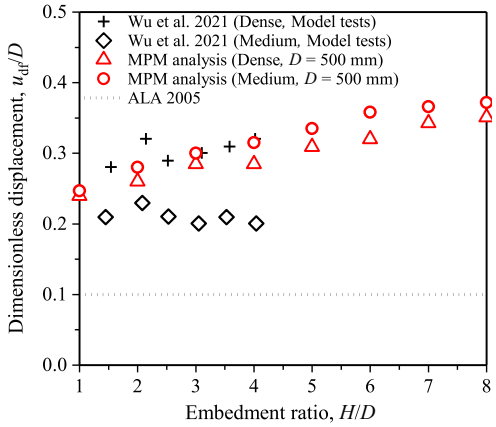

Fig. 19. Comparison of normalized pipe displacement corresponding to the failure threshold versus embedment ratio.

capacity of pipes are further investigated through parameter analysis. The following conclusions can be made:

(1) The failure mechanisms in the sand are comprehensively affected by the relative density, pipe size and burial depth. The shear bands induced by the bearing capacity are relatively localized in medium sand rather than dense sand. As the burial depth and pipe diameter increase, the failure mechanism essentially shifts from a general pattern that tends to develop to the surface to a local and deep pattern due to the changes in stress levels. Under shallow burial conditions, the location of the failure surfaces can be approximately outlined by the log-spiral curves given in Prandtl's solution.

(2) The ultimate resistance exerted on pipes can be estimated reasonably using the bearing capacity formulas recommended by the current guidelines with an appropriate sand friction angle. The failure threshold suggested in the previous FE analyses might be underestimated to some extent due to the insufficient pipe offset. Compared with the recommended value of 0.1D in the guidelines, the yield displacement of the elastoplastic bearing spring may need to be increased to (0.2–0.3)D, indicating a weaker resistance response corresponding to the same pipe offset. This value also varies with the sand density and burial depth of the pipe.

(3) The scale effect analysis indicates that previous laboratory tests with relatively small diameter pipes would provide a conservative estimate of the bearing capacity for practical pipeline designs. However, this analysis is performed mainly based on the dependency of the stiffness and dilatancy responses on the stress level, without considering the effects of the size of sand grains on the reaction evolution. A multiscale modeling approach may be used to capture the force–displacement response related to the microscopic properties of sands.

(4) The difference in interface friction between sands and the pipeline with various coatings should also be considered for determining the properties of vertical bearing soil springs. Moreover, when using elastoplastic bearing springs to analyze the three-dimensional pipe-soil interaction, some correction of the spring parameters might be required because the significant soil deformation and flow near the fault plane or shear zone make it difficult to satisfy the plane strain condition.

Declaration of competing interest

The authors declare that they have no known competing financial interests or personal relationships that could have appeared to influence the work reported in this paper.

Acknowledgments

This work is financially supported by the National Natural Science Foundation of China (Grant Nos. 42225702, 42077235 and 41722209). The authors wish to express their special gratitude to Dong Liao of Zhejiang University for providing the Fortran code of the J_2 model and his great assistance in the model implementation. The authors also thank the Computational Dynamics Laboratory led by Professor Xiong Zhang at Tsinghua University for sharing the open source code MPM3D-F90.

Appendix A. Supplementary data

Supplementary data to this article can be found online at https://doi.org/10.1016/j.jrmge.2022.07.010.

References

Ajalloeian, R., Yu, H.S., Allman, M.A., 1996. Physical and mechanical properties of Stockton beach sand. In: Proceedings of 7th Australia New Zealand Conference on Geomechanics, Adelaide, Australia, pp. 60–65.

Akhtar, S., Li, B., 2020. Numerical analysis of pipeline uplift resistance in frozen clay soil considering hybrid tensile-shear yield behaviors. Int. J. Geosynth. Ground Eng. 6, 47.

ALA, 2005. Guidelines for the Design of Buried Steel Pipe. American Lifelines Alliance, ASCE.
Ansari, Y., Kouretzis, G., Sloan, S.W., 2018. Development of a prototype for modelling soil-pipe interaction and its application for predicting uplift resistance to buried pipe movements in sand. Can. Geotech. J. 55 (10), 1451–1474.
Bandara, S., Soga, K., 2015. Coupling of soil deformation and pore fluid flow using material point method. Comput. Geotech. 63, 199–214.
Bardenhagen, S.G., Brackbill, J.U., Sulsky, D., 2000. The material-point method for granular materials. Comput. Methods Appl. Mech. Eng. 187 (3–4), 529–541.
Bardenhagen, S.G., Kober, E.M., 2004. The generalized interpolation material point method. Comput. Model. Eng. Sci. 5 (6), 477–495.
Bažant, Z.P., Belytschko, T.B., Chang, T.P., 1984. Continuum theory for strain-softening. J. Eng. Mech. 110 (12), 1666–1692.
Bhandari, T., Hamad, F., Moormann, C., Sharma, K.G., Westrich, B., 2016. Numerical modelling of seismic slope failure using MPM. Comput. Geotech. 75, 126–134.
Boor, C.D., 1978. A Practical Guide to Splines. Applied Mathematical Sciences. Springer, New York, USA.
Courant, R., Friedrichs, K., Lewy, H., 1967. On the partial difference equations of mathematical physics. IBM J. Res. Dev. 11, 215–234.
Davis, E.H., 1968. Theories of plasticity and failure of soil masses. In: Soil Mechanics: Selected Topics, New York, USA, pp. 341–354.
Durgunoglu, H.T., Mitchell, J.K., 1973. Static Penetration Resistance of Soils. Space Sciences Laboratory, Berkeley, California.
Ganju, E., Galvis-Castro, A.C., Janabi, F., Prezzi, M., Salgado, R., 2021. Displacements, strains, and shear bands in deep and shallow penetration processes. J. Geotech. Geoenviron. Eng. 147 (11), 04021135.
Gan, Y., Sun, Z., Chen, Z., Zhang, X., Liu, Y., 2018. Enhancement of the material point method using B-spline basis functions. Int. J. Numer. Methods Eng. 113 (3), 411–431.
Guo, P.J., Stolle, D.F.E., 2005. Lateral pipe-soil interaction in sand with reference to scale effect. J. Geotech. Geoenviron. Eng. 131 (3), 338–349.
Janbu, N., 1963. Soil compressibility as determined by oedometer and triaxial tests. In: Proceedings of European Conference on Soil Mechanics and Foundation Engineering. ECSMFE), Wiesbaden, Germany, pp. 19–25.
Jung, J.K., O'Rourke, T.D., Argyrou, C., 2016. Multi-directional force-displacement response of underground pipe in sand. Can. Geotech. J. 53 (11), 1763–1781.
Kouretzis, G.P., Bouckovalas, G., 2019. Analysis of buried oil and gas pipelines crossing active faults: revisiting pipe-ground interaction. In: Proceedings of 7th International Conference on Earthquake Geotechnical Engineering, Rome, Italy, pp. 550–565.
Kouretzis, G.P., Karamitros, D.K., Sloan, S.W., 2015. Analysis of buried pipelines subjected to ground surface settlement and heave. Can. Geotech. J. 52 (8), 1058–1071.
Kouretzis, G.P., Krabbenhøft, K., Sheng, D.C., Sloan, S.W., 2014. Soil-buried pipeline interaction for vertical downwards relative offset. Can. Geotech. J. 51 (10), 1087–1094.
Li, H.J., Zhu, H.H., Li, Y.H., Zhang, C.X., Shi, B., 2022. Experimental study on uplift mechanism of pipeline buried in sand using high-resolution fiber optic strain sensing nerves. J. Rock Mech. Geotech. Eng. 14 (4), 1304–1318.
Li, X.S., 2002. A sand model with state-dependent dilatancy. Géotechnique 52 (3), 173–186.
Li, X.S., Dafalias, Y.F., 2000. Dilatancy for cohesionless soils. Géotechnique 50 (4), 449–460.
Li, X.S., Wang, Y., 1998. Linear representation of steady-state line for sand. J. Geotech. Geoenviron. Eng. 124 (12), 1215–1217.
Liang, W.J., Zhao, J.D., 2019. Multiscale modeling of large deformation in geomechanics. Int. J. Numer. Anal. Methods Geomech. 43 (5), 1080–1114.
Liao, D., Yang, Z.X., 2021. Effect of fabric anisotropy on bearing capacity and failure mode of strip footing on sand: an anisotropic model perspective. Comput. Geotech. 138, 104330.
Liao, D., Yang, Z.X., Xu, T.T., 2021. J_2-deformation-type soil model coupled with state-dependent dilatancy and fabric evolution: multiaxial formulation and FEM implementation. Comput. Geotech. 129, 103674.
Limnaiou, T., Tsifis, C., Bouckovalas, G., Chaloulos, Y., 2019. Effect of trench dimensions on the vertical resistance of pipelines embedded in stiff soils and rocks. In: Proc., 7th International Conf. On Earthquake Geotechnical Engineering, Rome, Italy, pp. 3617–3624.
Mallikarachchi, H., Soga, K., 2020. Post-localisation analysis of drained and undrained dense sand with a nonlocal critical state model. Comput. Geotech. 124, 103572.
Ni, P.P., Qin, X.G., Yi, Y., 2018. Numerical study of earth pressures on rigid pipes with tire-derived aggregate inclusions. Geosynth. Int. 25 (5), 494–506.
Phuong, N.T.V., van Tol, A.F., Elkadi, A.S.K., Rohe, A., 2016. Numerical investigation of pile installation effects in sand using material point method. Comput. Geotech. 73, 58–71.
PRCI, 2009. Guidelines for Constructing Natural Gas and Liquid Hydrocarbon Pipelines in Areas Subject to Landslide and Subsidence Hazards. RPCI Pipeline Research Council International Inc.
Qin, X.G., Ni, P.P., Du, Y.J., 2019. Buried rigid pipe-soil interaction in dense and medium sand backfills under downward relative movement: 2D finite element analysis. Transp. Geotech. 21.
Sloan, S.W., Booker, J.R., 2010. Integration of Tresca and Mohr-Coulomb constitutive relations in plane strain elastoplasticity. Int. J. Numer. Methods Eng. 33 (1), 163–196.
Steffen, M., Kirby, R.M., Berzins, M., 2008. Analysis and reduction of quadrature errors in the material point method (MPM). Int. J. Numer. Methods Eng. 76 (6), 922–948.
Steffen, M., Kirby, R.M., Berzins, M., 2010. Decoupling and balancing of space and time errors in the material point method (MPM). Int. J. Numer. Methods Eng. 82 (10), 1207–1243.
Sulsky, D., Zhou, S.J., Schreyer, H.L., 1995. Application of a particle-in-cell method to solid mechanics. Comput. Phys. Commun. 87, 236–252.
Trautmann, C.H., 1983. Behavior of Pipe in Dry Sand under Lateral and Uplift Loading. Ph.D. thesis. Cornell University, New York.
Wang, D.Y., Zhu, H.H., Wang, B.J., Shi, B., 2021. Performance evaluation of buried pipe under loading using fiber Bragg grating and particle image velocimetry techniques. Measurement 186, 110086.
White, D.J., Cheuk, C.Y., Bolton, M.D., 2008. The uplift resistance of pipes and plate anchors buried in sand. Géotechnique 58 (10), 771–779.
Wu, J.B., Kouretzis, G., Suwal, L., 2021. Bearing capacity mechanisms for pipes buried in sand. Can. Geotech. J. 58 (6), 834–847.
Yang, Z.X., Xu, T.T., Li, X.S., 2019. J_2-deformation type model coupled with state dependent dilatancy. Comput. Geotech. 105, 129–141.
Yao, C.F., He, C., Takemura, J., Feng, K., Guo, D.P., Huang, X., 2021. Active length of a continuous pipe or tunnel subjected to reverse faulting. Soil Dyn. Earthq. Eng. 148.
Yimsiri, S., Soga, K., Yoshizaki, K., Dasari, G.R., O'Rourke, T.D., 2004. Lateral and upward soil-pipeline interactions in sand for deep embedment conditions. J. Geotech. Geoenviron. Eng. 130 (8), 830–842.
Zhang, C.X., Zhu, H.H., Zhang, W., Li, H.J., Liu, W., 2022. Modeling uplift failure of pipes buried in sand using material point method. Tunn. Undergr. Space Technol. 119, 104203.
Zhang, D.Z., Ma, X., Giguere, P.T., 2011. Material point method enhanced by modified gradient of shape function. J. Comput. Phys. 230 (16), 6379–6398.
Zhang, X., Chen, Z., Liu, Y., 2017. The Material Point Method: a Continuum-Based Particle Method for Extreme Loading Cases. Academic Press, Oxford.
Zhu, F.Y., Clark, J.I., Phillips, R., 2001. Scale effect of strip and circular footings resting on dense sand. J. Geotech. Geoenviron. Eng. 127 (7), 613–621.

Dr. Honghu Zhu is currently a Professor at the School of Earth Sciences and Engineering and the Dean of the Institute of Earth Exploration and Sensing, Nanjing University, China. He holds a Ph.D. degree in Geotechnical Engineering from the Hong Kong Polytechnic University. His research interests lie primarily in fiber optic monitoring and stability analysis of geoengineering problems, with particular emphasis on interface behaviors. His research outputs have been transformed and applied in many projects, such as landslide monitoring in the Three Gorges Reservoir area, debris flow prevention and control in Wenchuan earthquake area, and structural health monitoring of the Pearl River Delta water conveyance tunnel. In the past decade, he has co-authored 2 books, 12 patents, and over 80 journal and conference papers. He is the recipient of the 1st-class Prize of National Scientific & Technological Progress Award of China of 2018. He served as an editorial board member of *Journal of Rock Mechanics and Geotechnical Engineering* (JRMGE) and *International Journal of Geosynthetics and Ground Engineering*.